ACS Photonics

Open Access

pubs.acs.org/journal/apchd5

Article

UV-Transparent Bifocal Meta-Lens for Spin-Space Multiplexing with High-Quality Aluminum Nitride Buffer

Tien-Chiu Chen, Zhi-Yan Lin, Wen-Hsuan Hsieh, Ming Lun Tseng, Tien-Chang Lu, and Chia-Yen Huang*

Cite This: *ACS Photonics* 2025, 12, 1235−1242

Read Online

ACCESS | Metrics & More | Article Recommendations

ABSTRACT: We designed and fabricated the first bifocal meta-lens with a high-quality AlN buffer on a sapphire substrate. According to the ellipsometry measurement, the refractive index of AlN is above 2.2, and the extinction coefficient is below 0.002 in the whole ultraviolet (UV) spectral region. The meta-atom library consists of nanofins with near-unity half-wavelength plate efficiency with a full 2π coverage in the effective propagation phase of the converted spin. Two independent lens profiles for right-circularly polarized (RCP) and left-circularly polarized (LCP) spins are constructed within a single closely packed metasurface by simultaneous modulation of the geometric phase and the effective propagation phase of the converted spin. The fabricated 100 μm × 100 μm bifocal meta-lens showed a ∼1.3 μm full width at half-maximum at both foci at 365 nm, which is close to the theoretical prediction. When the incident light is pure LCP or RCP spin, the signal-to-noise ratio between the two foci is above 40. The bifocal meta-lens can be applied to spin demultiplexing in proximity and space-division multiplexing in the UV spectral region.

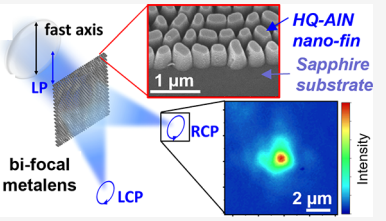

KEYWORDS: *ultraviolet, meta-lens, aluminum nitride, multiplexing, photonic spin*

INTRODUCTION

Ultraviolet (UV, λ = 200−400 nm) light has a wide variety of applications, from curing, sterilization, and medical treatment to manufacturing.[1−4] Many applications use UV emitters as an information carrier. For example, mask-less laser direct lithography and photon-induced additive manufacturing use UV photons to code the spatial information into UV-sensitive materials.[5−7] Solar-blind communication and non-line-of-sight communication also transmit signals in deep-UV spectral regions.[8−10] The UV single-photon emitter is also a pivotal component in developing quantum information technology under room temperature.[11−14] Metasurfaces have been a rapidly emerging technology in the past decade because of their unmet functionalities in conventional optic elements. The metasurface tailors the wavefront and polarization of the incident light by the two-dimensional phase profiles encoded in subwavelength meta-atom arrays. Deflection, focusing, vortex formation, hologram, and many other light manipulations have been demonstrated in a broad range of spectral regions, from visible light to terahertz.[15−20] However, few reports of metasurfaces working in the UV spectral region exist. UV-transparent wide bandgap materials usually have a low refractive index and are often chemically robust. The major bottleneck for realizing an efficient metasurface in the UV spectral region is how to assemble and fabricate the subwavelength meta-atoms with 2π phase coverage. Nb_2O_5 (E_g = 3.65 eV) and HfO_2 (E_g = 5.7 eV) metasurfaces were fabricated via the Damascene process assisted by atomic layer deposition.[21,22] Kim et al. embedded ZrO_2 (E_g ∼ 5.8 eV) nanoparticles in UV-curable resin to facilitate processing at the cost of the lower averaged refractive index.[23] The UV metasurface with other-material choices (SiN_x, MgO···etc.) remains at the design level.[24−27] Only the Ta_2O_5 (E_g ∼ 3.7 eV) metasurface was fabricated via direct pattern-and-etching on the sputtered film.[28] AlN was considered a potential candidate for UV metasurfaces due to its ultrawide bandgap (E_g ∼ 6.1 eV) and the established dry-etching technique.[29,30] However, AlN metasurface studies are either a pure numerical design or experimental demonstration of micrometer-scale concentric zone plates.[31,32] The lack of the more versatile AlN metasurface demonstration might be attributed to the absence of a high-quality and homogeneous AlN dielectric layer on the nanometer scale. Recently, novel high-quality AlN buffer technology on sapphire has been flourishing as the growth template for ultraviolet-C light-emitting diodes.[33−38] In addition, its low threading dislocation density and atomically flat surface make it very promising for efficient metasurfaces in the UV spectral region. Figure 1a and 1b respectively plots the refractive index (n) and extinction coefficient (k) of our AlN

Received: December 23, 2024
Revised: January 29, 2025
Accepted: January 29, 2025
Published: February 4, 2025

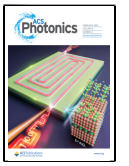

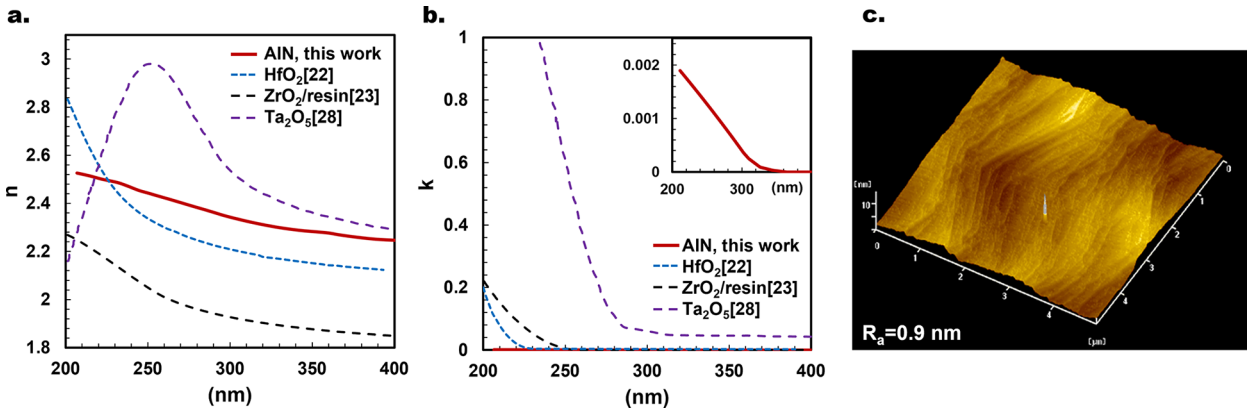

Figure 1. (a) Refractive index (n) and (b) extinction coefficient (k) of the AlN buffer and other published materials for metasurfaces in the UV spectral region. (c) 5 μm × 5 μm AFM image of high-quality AlN buffer; the roughness (R_a) is marked in the bottom-left corner.

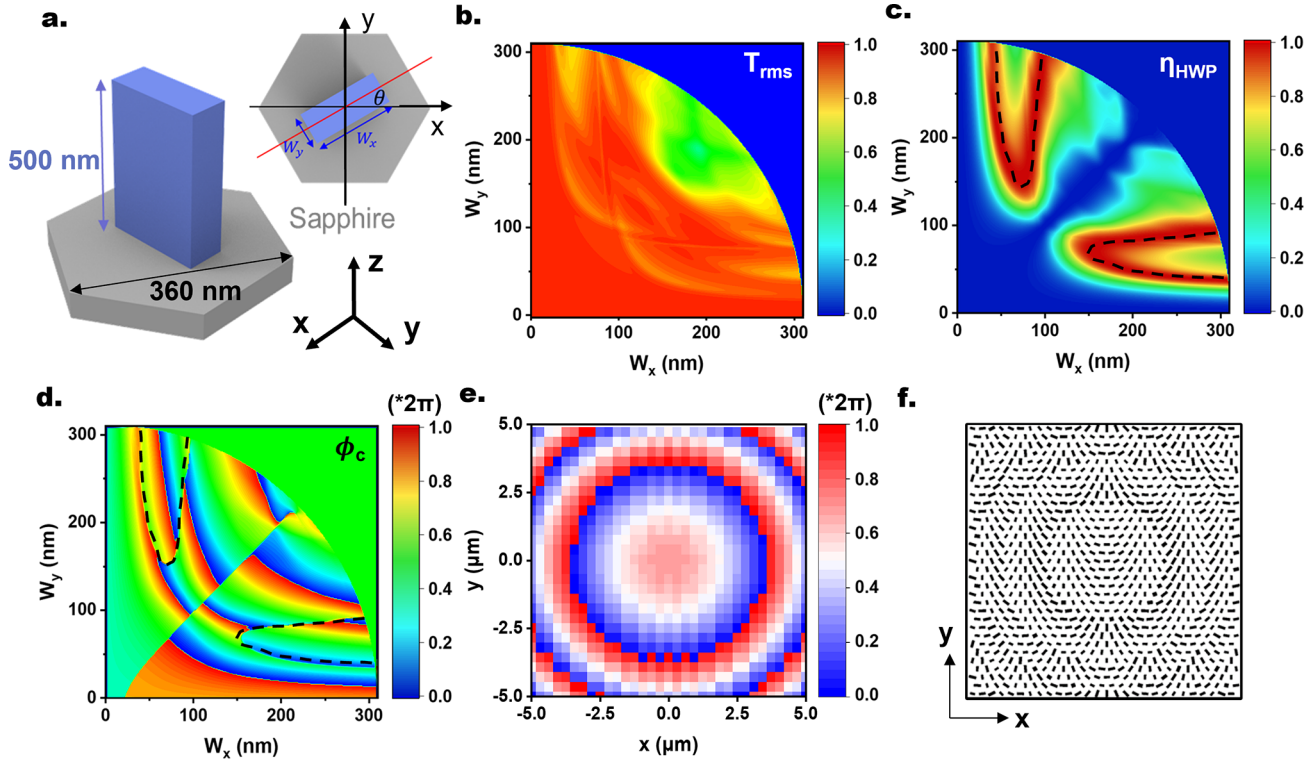

Figure 2. (a) Schematic structure of the AlN meta-atom nanofin. The calculated (b) T_{rms}, (c) η_{HWP}, and (d) ϕ_c mapping in W_x and W_y. The back dashed contours in (c) and (d) represent the collection of meta-atoms with $\eta_{HWP} > 0.99$. (e) Pixelated $\phi_c(x,y)$ profile and (f) final meta-lens pattern from eqs (9) and (10) with F = 20 μm and x_0 = 3 μm.

buffer measured by ellipsometry in comparison with those of selected materials in other UV metasurface studies. n of AlN ranges from 2.25 to 2.52, and most importantly, k is below 0.002 down to 210 nm, which is much more transparent than materials published in other metasurfaces working in the UV spectral region. For example, Ta_2O_5 from ref 28 possessed a higher refractive index than AlN, but k is non-negligible (>0.05) in the whole UV spectral region. HfO_2[22] and ZrO_2/resin[23] composite is transparent down to 250 nm, and then k rises toward the deeper UV spectral region. Figure 1c is the atomic force microscopy (AFM) image of the AlN buffer surface. Terrace morphology in atomic scale implies its homogeneity on a nanometer scale and epitaxial-grade smoothness.

In this report, we demonstrated the first bifocal AlN meta-lens that can focus left-circularly polarized (LCP) light and right-circularly polarized (RCP) light on two vicinal foci. We introduce the concept of half-wavelength plate efficiency (η_{HWP}) via Jones matrix formalism to construct the library of AlN rectangular nanofins with an optimized conversion efficiency. Simulation and optical characterization revealed that the designed bifocal meta-lens possesses a high transmittance, near-diffraction-limited focusing, and a high extinction ratio between orthogonal spins at the wavelength 365 nm (i-line). The results implied that the novel AlN buffer could be the optimal material for metasurfaces in the whole UV. They paved the way toward capacity enhancement for UV-based manufacturing and communication applications by space-spin multiplexing and demultiplexing.[39,40]

https://doi.org/10.1021/acsphotonics.4c02575
ACS Photonics 2025, 12, 1235−1242

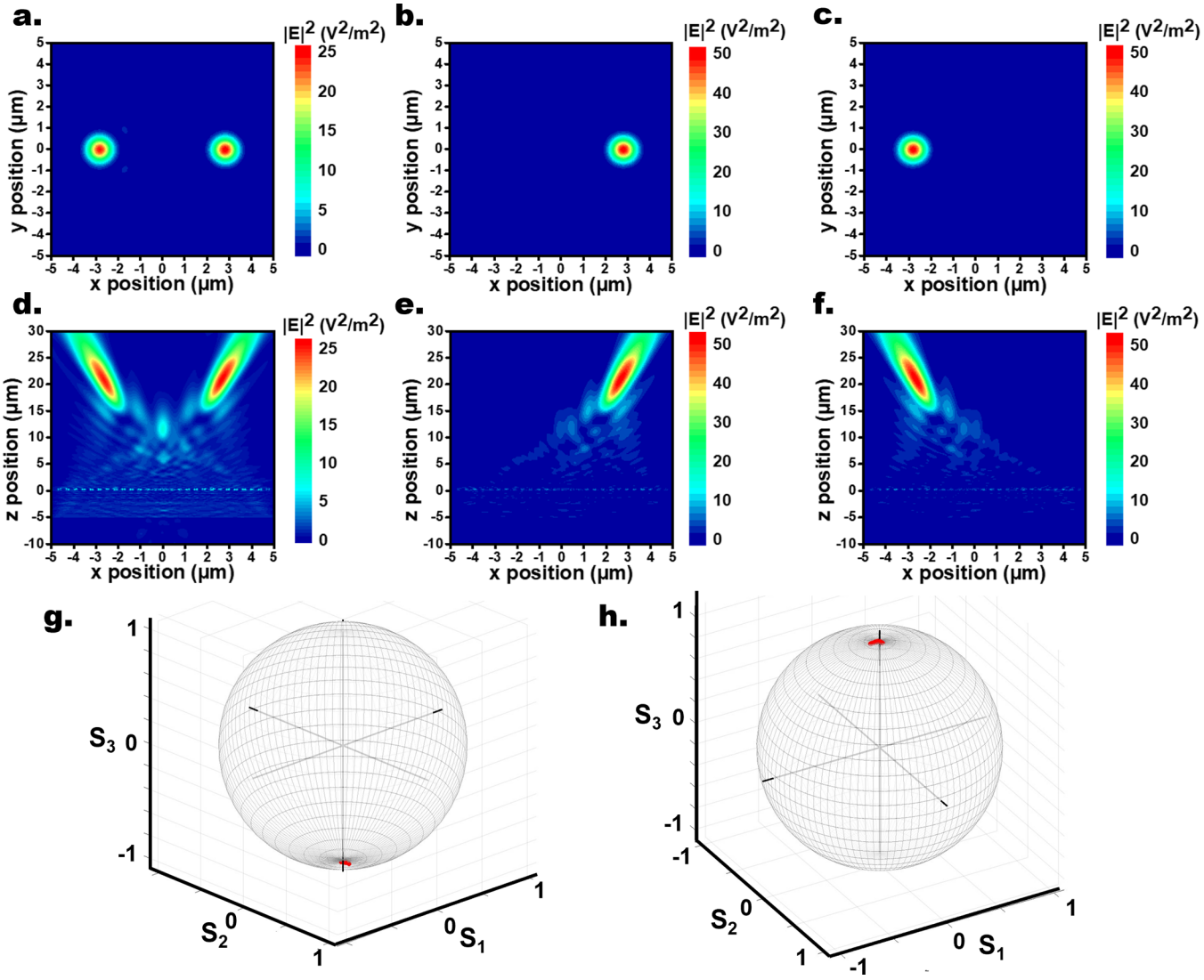

Figure 3. Absolute electric field distribution at the focal plane with (a) LP, (b) RCP, and (c) LCP light incidence. Their corresponding mapping on the vertical $x-z$ cross-sectional plane is plotted in (d) to (f). Mapping the Stokes vectors of the electric field within the half-intensity contour with a (g) RCP and (h) LCP incident light. The coordinate represents a pure (g) LCP and (h) RCP at the focus, respectively.

PRINCIPLE OF BIFOCAL META-LENS DESIGN

To route photons with opposite spins independently with only one set of closely packed meta-atoms, the propagation and geometric phases of polarization-selective meta-atoms must be modulated simultaneously to fulfill the degree of freedom.[41,42] The AlN rectangular nanofin schematic illustration is in Figure 2a. For meta-lens in the UV spectral region, the lattice constant is intentionally chosen to be close to the target wavelength due to practical processing limitations. Therefore, we adopted the hexagonal lattice for its higher filling factor to suppress the efficiency loss due to the Nyquist limitation. The lattice constant of the hexagonal lattice is set to 360 nm, and the height is set to 500 nm. The Jones matrix presentation of light passing through the nanofin with the basis of the x- and y-polarized unit electric field is written as eq (1):

$$\begin{bmatrix} E_{x,\mathrm{out}} \\ E_{y,\mathrm{out}} \end{bmatrix} = \mathrm{R}(-\theta)\mathrm{MR}(\theta)\begin{bmatrix} E_{x,\mathrm{in}} \\ E_{y,\mathrm{in}} \end{bmatrix} \quad ((1))$$

where θ is the rotation angle between the reference axes and the principal axes of ordinary ray (o-ray) and extraordinary ray (e-ray), R is the rotational matrix, and M is the propagation matrix. If we change the basis to unit LCP and RCP spins, the matrix becomes eq (2):

$$\begin{bmatrix} E_{\mathrm{L,out}} \\ E_{\mathrm{R,out}} \end{bmatrix} = \begin{bmatrix} \frac{T_o e^{i\varphi_o} + T_e e^{i\varphi_e}}{2} & \frac{T_o e^{i\phi_o} - T_e e^{i\varphi_e}}{2} e^{-i2\theta} \\ \frac{T_o e^{i\varphi_o} - T_e e^{i\varphi_e}}{2} e^{i2\theta} & \frac{T_o e^{i\varphi_o} + T_e e^{i\varphi_e}}{2} \end{bmatrix} \begin{bmatrix} E_{\mathrm{L,in}} \\ E_{\mathrm{R,in}} \end{bmatrix} \quad ((2))$$

where T_o/T_e is the real-valued electric field transmissivity and ϕ_o/ϕ_e is the propagation phase of the o-ray/e-ray, respectively. The T_o and ϕ_o of a nanofin with given W_x and W_y are calculated with Reticolo-RCWA implements by assuming the polarization of the plane wave to be linearly polarized along the reference x-axis. The T_e and ϕ_e for e-ray are obtained by symmetry operation by transposing W_x and W_y of the corresponding T_o and ϕ_o.

https://doi.org/10.1021/acsphotonics.4c02575
ACS Photonics 2025, 12, 1235−1242

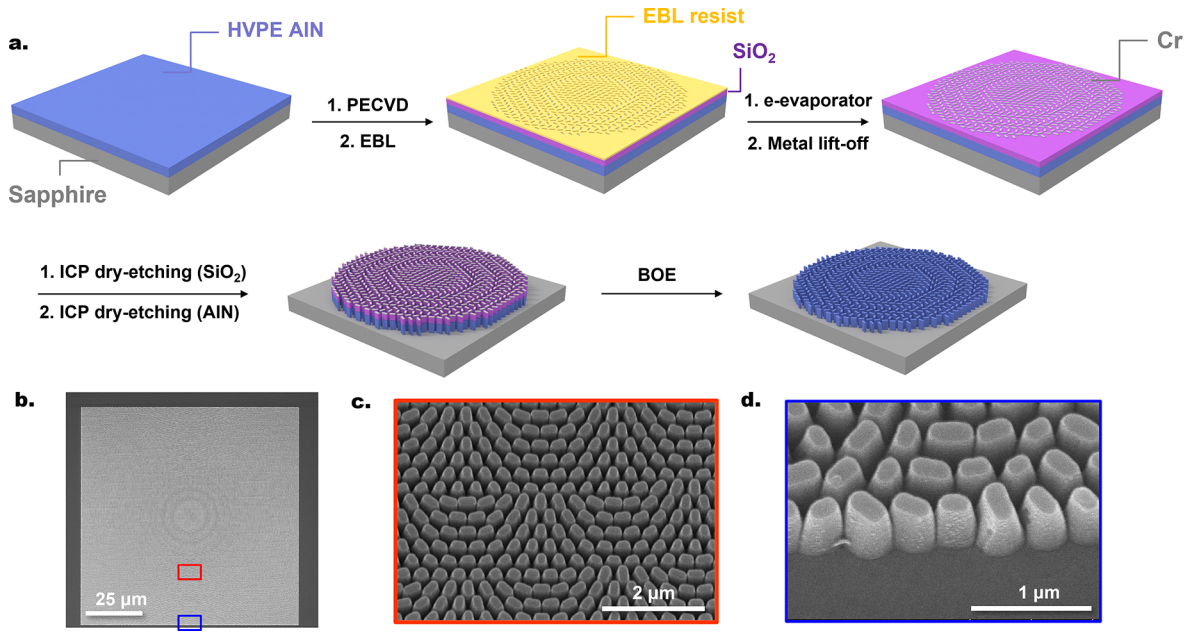

Figure 4. (a) Schematic process flow of the AlN bifocal meta-lens. The SEM (b) top view and (c) bird view in the field and (d) bird view at the edge of the 100 μm × 100 μmAlN bifocal meta-lens. The red and blue perimeters indicated the position of parts (c) and (d) in (b).

The matrix can be further simplified by introducing the root-mean-square transmissivity (T_{rms}) and half-wavelength plate efficiency (η_{HWP}) in eqs (3) and (4):

$$T_{rms} = \sqrt{\frac{T_e^2 + T_o^2}{2}} \tag{3}$$

$$\eta_{HWP}^2 = \frac{2T_c^2}{T_o^2 + T_e^2} = \frac{1}{2} - \frac{T_e T_o}{T_o^2 + T_e^2}\cos(\varphi_o - \varphi_e) \tag{4}$$

After substituting them to eq (2), it yields eq (5):

$$\begin{bmatrix} E_{L,out} \\ E_{R,out} \end{bmatrix} = T_{rms} \begin{bmatrix} \sqrt{1-\eta_{HWP}^2}\, e^{i\varphi_u} & \eta_{HWP} e^{i(\varphi_c - 2\theta)} \\ \eta_{HWP} e^{i(\varphi_c + 2\theta)} & \sqrt{1-\eta_{HWP}^2}\, e^{i\varphi_u} \end{bmatrix} \begin{bmatrix} E_{L,in} \\ E_{R,in} \end{bmatrix} \tag{5}$$

ϕ_u/ϕ_c is the effective propagation phase for the unconverted/converted spin, which can be evaluated by eqs (6) and (7).

$$\varphi_u = Arg(T_o e^{i\varphi_o} + T_e e^{i\varphi_e}) \tag{6}$$

$$\varphi_c = Arg(T_o e^{i\varphi_o} - T_e e^{i\varphi_e}) \tag{7}$$

From eq (4), $\eta_{HWP} = 1$ when T_o=T_e and $\phi_o - \phi_e = \pm\pi$, which is equivalent to the function of a half-wavelength plate (HWP). Equation (5) can be further reduced to eq (8) when $\eta_{HWP} = 1$:

$$\begin{bmatrix} E_{L,out} \\ E_{R,out} \end{bmatrix} = T_{rms} \begin{bmatrix} E_{R,in} e^{i(\varphi_c - 2\theta)} \\ E_{L,in} e^{i(\varphi_c + 2\theta)} \end{bmatrix} = T_{rms} \begin{bmatrix} E_{R,in} e^{i\varphi_R} \\ E_{L,in} e^{i\varphi_L} \end{bmatrix} \tag{8}$$

For brevity, the collection of meta-atoms with a unity η_{HWP} is named the HWP ensemble. From eq (8), the phase profiles seen by LCP light (ϕ_L) and RCP light (ϕ_R) can be arbitrarily synthesized if ϕ_c of the HWP ensemble covers 2π. One light spin could see an independent phase profile and then switch to the other spin. Figure 2b–d maps T_{rms}, η_{HWP}, and ϕ_c as a function of W_x/W_y, respectively. The black dashed contour in (c) and (d) is the HWP ensemble contour with $\eta_{HWP} > 0.99$, and fortunately, ϕ_c covers 2π along the contour, and the average T_{rms} is decent (>85%). With a given ϕ_c, W_x and W_y can be retrieved from Figure 2d. Equations (9) and (10) are two meta-lens profiles with a given focal length (F) and a shift of foci along the x-axis (x_0) from the optical axis for RCP and LCP spin:

$$\varphi_R(x, y) = \frac{2\pi}{\lambda}(F - \sqrt{F^2 + (x - x_0)^2 + y^2}) \tag{9}$$

$$\varphi_L(x, y) = \frac{2\pi}{\lambda}(F - \sqrt{F^2 + (x + x_0)^2 + y^2}) \tag{10}$$

where F = 24 μm and x_0 = 3 μm. Figure 2e shows the pixelated $\phi_c(x, y)$ by $\phi_c = (\phi_L + \phi_R)/2$. With retrieved W_x, W_y, and $\theta = (\phi_L - \phi_R)/4$, a 10 μm × 10 μm bifocal meta-lens pattern can be generated as in Figure 2f.

Finite-Difference Time-Domain (FDTD) Simulation Verification. The generated meta-lens structures were imported into Ansys Lumerical FDTD for verification. To balance the calculation capacity and device functionality, the dimension of meta-lens was set to be a 10 μm × 10 μm square surrounded by perfectly matched layers (PMLs). The light propagated along the + z axis from the substrate toward the air. The AlN/sapphire interface is set to be the z = 0 plane. Vertical PMLs were positioned at z = −5 and 30 μm. The incident beams are plane waves with unity amplitude (1 V/m) from the sapphire substrate, but the polarization was set to be linearly polarized (LP), RCP, or LCP. The intensity distributions at the focal plane are plotted in Figure 3a–c, and the distributions at the vertical cross-section through foci are plotted in Figure 3d,e. The simulated foci were consistent with the designed values (F = 24 μm, x_0 = 3 μm). Under LP light incidence, the field intensities at both foci are equal (~25 V^2/m^2), and their value is half of that under pure RCP or LCP incidence. It is worth noticing that under a pure RCP or LCP

https://doi.org/10.1021/acsphotonics.4c02575
ACS Photonics 2025, 12, 1235−1242

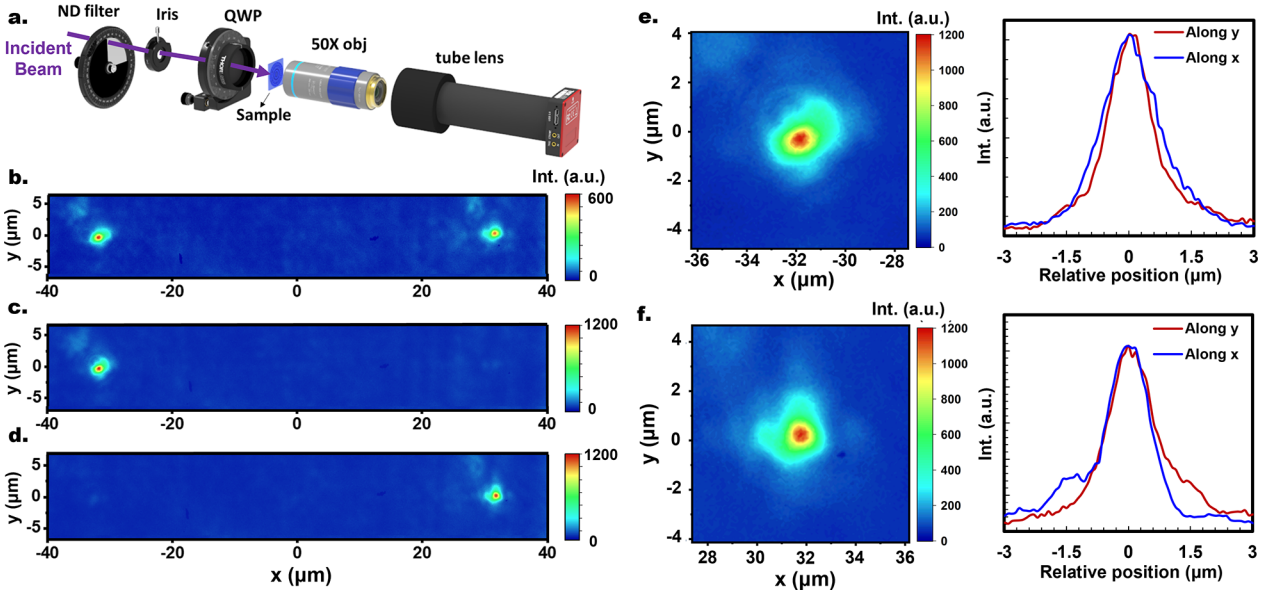

Figure 5. (a) Schematic setup for the near-field intensity measurement at the focal plane. The CCD images when the incident light is (b) LP, (c) LCP, and (d) RCP. The magnified images near the focal point of (c) and (d) are in (e) and (f), respectively. The cross-sectional profiles through the apex are plotted beside the color mapping.

light incidence, the intensities at the opposite focal point and the zero-order central point are minimal. The distinctive signal-to-background ratio implied a full polarization conversion due to the intentional selection of the HWP ensemble. The electric fields within the half-intensity maximum contour in Figure 3b,c were picked to calculate their Stokes vector, and their coordinates are presented on the Poincare's sphere in Figure 3g,h. The absolute values of S_3 are all above 0.99, implying a pure spin after focusing on their foci with a spin inversion.

Fabrication Process. The 500−550 nm high-quality AlN buffer layers on 2 in. (001) flat sapphire substrate were purchased from Sumitomo Electronics Inc. AlN is deposited via hydride vapor phase epitaxy. The sapphire substrate's backside is polished to a mirror-like surface. For ease of alignment in the experiment, we scaled the bifocal meta-lens with 10 times in total width (100 μm), F (240 μm), and x_0 (30 μm) of the FDTD simulations to retain the same level of numerical aperture (NA ∼ 0.2). The top-side fabrication process is schematically illustrated in Figure 4a. A 300 nm SiO_2 was deposited on AlN by plasma-enhanced chemical vapor deposition (PECVD). 140 nm poly(methyl methacrylate) (PMMA-A3) resist was spin-coated as the positive resist electron beam lithography (EBL). Rectangular holes on PMMA are formed after development. 40 nm Cr was deposited on the patterned PMMA with the e-gun evaporator; then, it was patterned via the lift-off process in acetone. The pattern is transferred from Cr to SiO_2 hardmask with CHF_3/Ar mixture in reactive ion etching (RIE) system; then it is further transferred to AlN with the Cl_2/BCl_3/Ar mixture in the RIE system as well. Figure 4b−d shows the scanning electron microscopy images of the final bifocal meta-lens under different magnifications and positions. The sidewall is smooth and slightly tilted from verticality due to the finite selectivity of the hard mask. The corners are inevitably rounded because of the lateral dry etching from the orthogonal directions.

RESULTS AND DISCUSSION

The schematic measurement setup is shown in Figure 5a. A fully integrated wavelength-tunable optical parametric oscillator (Horizon SL-EX, Amplitude) was used as the incident light source. The incident light is horizontally LP with an extinction ratio >100 and a divergence angle <2 mrad. The beam size was narrowed by a 300 μm-diameter iris first, and then the polarization state was modulated by a rotational QWP (ThorLabs). The meta-lens was mounted on a homemade 3D-printed fixture perpendicular to the optical axis. The NUV-transparent 50× infinity-corrected objective lens (Mitutoyo, f = 200 μm), tube lens, and charge-coupled display (CDD, Ophir) were attached to the motorized linear translational stage along the optical axis. The bifocal AlN meta-lens and the 50-times magnification objective lens shared a common focal plane to magnify and project the near-field intensity. The zero position is set when the edge of the meta-lens is on focus under ambient illumination, and the focal point is determined when the intensity profile is at its narrowest case. The tunable ND filter before the iris prevents the signal saturation on CCD.

The CCD images with different incident polarizations are shown in Figure 5b−f. The separation between measured foci is 64 μm, which is close to the designed value (60 μm). The discrepancy might originate from the limited accuracy and precision in the process, for example, the actual buffer thickness, the rounded corners, and the slightly tilted sidewall of the meta-atom. The measured full-width at half-maximum (FWHM) is around 1.3 μm, which is already close to the simulation-predicted results with the same NA (1.12 μm). Under LP light incidence, the intensities at two foci are comparable; when the incident light is tuned to LCP or RCP, the peak intensity nearly doubles, as the simulations predicted. Under LCP/RCP light incidence, the signal at the opposite focal can still be observable, but it is ∼40 times weaker than that at the assigned focal point. We inferred the weak signal at the opposite focal point to the finite extinction ratio of the laser light and the nonideal conversion efficiency of the QWP.

https://doi.org/10.1021/acsphotonics.4c02575
ACS Photonics 2025, 12, 1235−1242

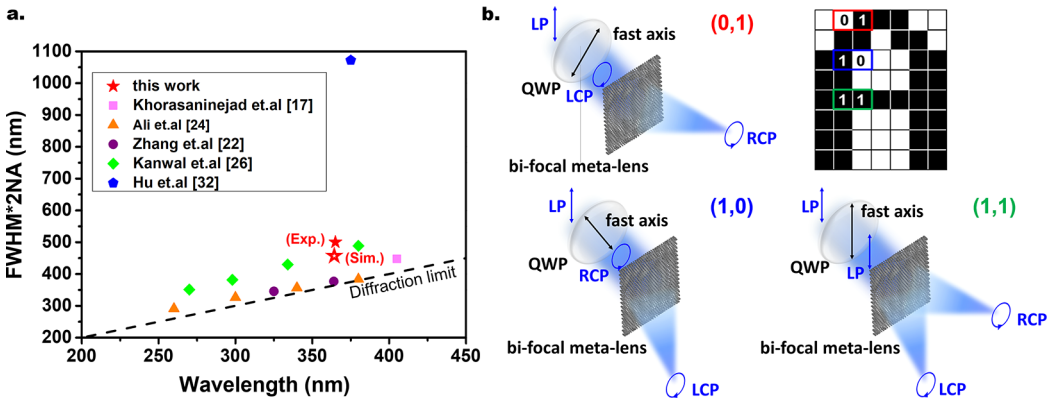

Figure 6. (a) Benchmark of FWHMs of meta-lens in the UV spectral region. (b) Mechanism of spin-space multiplexing with a QWP and bifocal meta-lens. When the fast axis of QWP is parallel or ±45° to the linear polarization of the laser, the optical energy will be focused on both pixels as the (1,1) state in red or only on the left or right pixel as the (1,0) or (0,1) state in blue and green, respectively.

Figure 6a summarizes the normalized FWHMs (FWHM × 2NA) of the reported meta-lens in the UV spectral region. Even in theoretical simulation, the normalized FWHM (hollow star) is 1.2 times higher than the diffraction limit. The measured FWHM (solid star) is 1.12 times higher than the simulated value, which is attributed to the limited dimensional accuracy of meta-atoms after processing. In order to acquire full 2π coverage of ϕ_c in the HWP ensemble, we adopted a lattice constant (360 nm), which is close to the target wavelength. The relatively low spatial phase sampling rate limited the ultimate resolution of the bifocal meta-lens. Single-focal AlN meta-lens with a smaller lattice constant and a diffraction-limited performance will be revealed elsewhere. Nevertheless, such AlN bifocal meta-lens demonstrates a strong potential for spin-space multiplexing for UV-based direct lithography and additive layer manufacturing applications. The bifocal meta-lens routes the LCP/RCP component of light into vicinal miniature channels for independent processing. Figure 6b illustrates the capacity enhancement mechanism with the bifocal meta-lens and a polarization modulator, such as a rotational QWP or a Pockels cell. In the conventional scenario, the 1/0 signal of one pixel can be encoded by the on/off state of the laser in one shot. With the bifocal meta-lens and the polarization modulator, the information on two parallel pixels can be delivered simultaneously. If the incident LP light stays unmodulated, the signal for both pixels will be 1; if the incident light is modulated to the RCP or LCP spin, the information will be 1 for one pixel and 0 for the other, and apparently, 0 for both pixels when the laser is off. Therefore, signals of two pixels can be delivered in one shot after a decent synchronization between the incident laser power and polarization modulator.

CONCLUSIONS

In conclusion, high-quality AlN buffer on sapphire is a powerful candidate for a UV metasurface because of its high refractive index and low absorption in the whole UV spectral region. Independent wavefront manipulation of RCP and LCP light spin with a high conversion efficiency and signal-to-noise ratio can be achieved by building the metasurface with the HWP ensemble with full coverage in the effective propagation phases. In this report, we designed and fabricated a bifocal meta-lens working at 365 nm using the proposed methodology, and the experimental results agree well with the simulation prediction well. The UV meta-lens can enhance the bandwidth or throughput of UV-based communication or processing techniques. The same design methodology could also be adopted for applications in other spectral regions.

ASSOCIATED CONTENT

Data Availability Statement

The data supporting the plots within this paper and other study findings are available from the corresponding author upon reasonable request.

AUTHOR INFORMATION

Corresponding Author

Chia-Yen Huang − *Department of Photonics, National Yang Ming Chiao Tung University, Hsinchu 30010, Taiwan;* orcid.org/0000-0003-0844-1903; Email: cyhuang06@nycu.edu.tw

Authors

Tien-Chiu Chen − *Department of Photonics, National Yang Ming Chiao Tung University, Hsinchu 30010, Taiwan*

Zhi-Yan Lin − *Department of Photonics, National Yang Ming Chiao Tung University, Hsinchu 30010, Taiwan*

Wen-Hsuan Hsieh − *Department of Photonics, National Yang Ming Chiao Tung University, Hsinchu 30010, Taiwan*

Ming Lun Tseng − *Institute of Eelectronics, National Yang Ming Chiao Tung University, Hsinchu 30010, Taiwan;* orcid.org/0000-0003-0418-8162

Tien-Chang Lu − *Department of Photonics, National Yang Ming Chiao Tung University, Hsinchu 30010, Taiwan;* orcid.org/0000-0003-4192-9919

Complete contact information is available at: https://pubs.acs.org/10.1021/acsphotonics.4c02575

Funding

This work was financially supported by the National Science and Technology Council (NTSC) of Taiwan under Contract No. NTSC-113-2628-E-A49-008.

Notes

The authors declare no competing financial interest.

REFERENCES

(1) Savage, N. Ultraviolet lasers. *Nat. Photonics* **2007**, *1* (2), 83−85.

(2) Kneissl, M.; Seong, T.-Y.; Han, J.; Amano, H. The emergence and prospects of deep-ultraviolet light-emitting diode technologies. *Nat. Photonics* **2019**, *13* (4), 233−244.

(3) Endruweit, A.; Johnson, M. S.; Long, A. C. Curing of composite components by ultraviolet radiation: A review. *Polym. Compos.* **2006**, *27* (2), 119−128.
(4) Lee, E.; Koo, J.; Berger, T. UVB phototherapy and skin cancer risk: A review of the literature. *Int. J. Dermatol.* **2005**, *44* (5), 355−360.
(5) de Beer, M. P.; van der Laan, H. L.; Cole, M. A.; Whelan, R. J.; Burns, M. A.; Scott, T. F. Rapid, Continuous additive manufacturing by volumetric polymerization inhibition patterning. *Sci. Adv.* **2019**, *5* (1), No. eaau8723.
(6) Bernardeschi, I.; Ilyas, M.; Beccai, L. A Review on Active 3D Microstructures via Direct Laser Lithography. *Adv. Intell. Syst.* **2021**, *3* (9), No. 2100051.
(7) Guijt, R. M.; Breadmore, M. C. Maskless photolithography using UV LEDs. *Lab Chip* **2008**, *8* (8), 1402.
(8) Memon, M. H.; Yu, H.; Jia, H.; Fang, S.; Wang, D.; Zhang, H.; Xiao, S.; Kang, Y.; Ding, Y.; Gong, C.; Sun, H. Quantum Dots Integrated Deep-Ultraviolet Micro-LED Array Toward Solar-Blind and Visible Light Dual-Band Optical Communication. *IEEE Electron Device Lett.* **2023**, *44* (3), 472.
(9) He, R.; Liu, N.; Gao, Y.; Chen, R.; Zhang, S.; Yuan, H.; Duo, Y.; Xu, J.; Ji, X.; Yan, J.; Wang, J.; Liu, J.; Li, J.; Wei, T. Monolithically integrated UVC AlGaN-based multiple quantum wells structure and photonic chips for solar-blind communications. *Nano Energy* **2022**, *104* (A), No. 107928.
(10) Xu, Z.; Sadler, B. M. Ultraviolet Communications: Potential and State-Of-The-Art. *IEEE Commun. Mag.* **2008**, *46* (5), 67−73.
(11) Bourrellier, R.; Meuret, S.; Tararan, A.; Stéphan, O.; Kociak, M.; Tizei, L. H. G.; Zobelli, A. Bright UV Single Photon Emission at Point Defects in h-BN. *Nano Lett.* **2016**, *16* (7), 4317.
(12) Aharonovich, I.; Englund, D.; Toth, M. Solid-state single-photon emitters. *Nat. Photonics* **2016**, *10* (9), 631−641.
(13) Chen, L.; Sheng, B.; Sheng, S.; Wang, P.; Sun, X.; Li, D.; Wang, T.; Tao, R.; Liu, S.; Chen, Z.; Ge, W.; Shen, B.; Wang, X. Room Temperature Triggered Single Photon Emission from Self-Assembled GaN/AlN Quantum Dot in Nanowire. *Adv. Funct. Mater.* **2022**, *32* (47), No. 2208340.
(14) Arakawa, Y.; Holmes, M. J. Progress in quantum-dot single photon sources for quantum information technologies: A broad spectrum overview. *Appl. Phys. Rev.* **2020**, *7* (2), No. 021309.
(15) Yu, N.; Capasso, F. Flat optics with designer metasurfaces. *Nat. Mater.* **2014**, *13* (1), 139−150.
(16) Chen, H.-T.; Taylor, A. J.; Yu, N. A review of metasurfaces: physics and applications. *Rep. Prog. Phys.* **2016**, *79* (7), No. 076401.
(17) Khorasaninejad, M.; Chen, W. T.; Devlin, R. C.; Oh, J.; Zhu, A. Y.; Capasso, F. Metalenses at visible wavelengths: Diffraction-limited focusing and subwavelength resolution imaging. *Science* **2016**, *352* (6290), 1190−1194.
(18) Yang, Q.; Gu, J.; Wang, D.; Zhang, X.; Tian, Z.; Ouyang, C.; Singh, R.; Han, J.; Zhang, W. Efficient flat metasurface lens for terahertz imaging. *Opt. Express* **2014**, *22* (21), 25931−25939.
(19) John-Herpin, A.; Tittl, A.; Kühner, L.; Richter, F.; Huang, S. H.; Shvets, G.; Oh, S.-H.; Altug, H. Metasurface-Enhanced Infrared Spectroscopy: An Abundance of Materials and Functionalities. *Adv. Mater.* **2022**, *35* (34), No. 2110163.
(20) Chen, S.; Cai, Y.; Li, G.; Zhang, S.; Cheah, K. W. Geometric metasurface fork gratings for vortex-beam generation and manipulation. *Laser Photonics Rev.* **2016**, *10* (2), 322−326.
(21) Huang, K.; Deng, J.; Leong, H. S.; Yap, S. L. K.; Yang, R. B.; Teng, J.; Liu, H. Ultraviolet metasurfaces of ≈80% efficiency with antiferromagnetic resonances for optical vectorial anti-counterfeiting. *Laser Photonics Rev.* **2019**, *13* (5), No. 1800289.
(22) Zhang, C.; Divitt, S.; Fan, Q.; Zhu, W.; Agrawal, A.; Lu, Y.; Xu, T.; Lezec, H. J. Low-loss metasurface optics down to the deep ultraviolet region. *Light: Sci. Appl.* **2020**, *9* (3), 55.
(23) Kim, J.; Kim, W.; Oh, D. K.; Kang, H.; Kim, H.; Badloe, T.; Kim, S.; Park, C.; Choi, H.; Lee, H.; Rho, J. One-step printable platform for high-efficiency metasurfaces down to the deep-ultraviolet region. *Light: Sci. Appl.* **2023**, *12* (3), 68.
(24) Ali, F.; Aksu, S. A hybrid broadband metalens operating at ultraviolet frequencies. *Sci. Rep.* **2021**, *11* (1), 2303.
(25) Guo, H.; Yue, S.; Wang, R.; Hou, Y.; Li, M.; Zhang, K.; Zhang, Z. Design of polarization-independent reflective metalens in the ultraviolet−visible wavelength region. *Nanomater.* **2021**, *11* (5), 1243.
(26) Kanwal, S.; Wen, J.; Yu, B.; Chen, X.; Kumar, D.; Kang, Y.; Bai, C.; Ubaid, S.; Zhang, D. Polarization insensitive, broadband, near diffraction-limited metalens in ultraviolet region. *Nanomater.* **2020**, *10* (8), 1439.
(27) Liu, M.; Xu, N.; Wang, B.; Qian, W.; Xuan, B.; Cao, J. Polarization independent and broadband achromatic metalens in ultraviolet spectrum. *Opt. Commun.* **2021**, *497* (1), No. 127182.
(28) Zhang, C.; Chen, L.; Lin, Z.; Song, J.; Wang, D.; Li, M.; Koksal, O.; Wang, Z.; Spektor, G.; Carlson, D.; Lezec, H. J.; Zhu, W.; Papp, S.; Agrawal, A. Tantalum pentoxide: A new material platform for high-performance dielectric metasurface optics in the ultraviolet and visible region. *Light: Sci. Appl.* **2024**, *13* (1), 23.
(29) Pinto, R. M. R.; Gund, V.; Calaza, C.; Nagaraja, K. K.; Vinayakumar, K. B. Piezoelectric aluminum nitride thin-films: A review of wet and dry etching techniques. *Microelectron. Eng.* **2022**, *257* (3), No. 111753.
(30) Liu, X.; Sun, C.; Xiong, B.; Niu, L.; Hao, Z.; Han, Y.; Luo, Y. Smooth etching of epitaxially grown AlN film by Cl_2/BCl_3/Ar-based inductively coupled plasma. *Vacuum* **2015**, *116* (6), 158−162.
(31) Gao, X.; Wan, R.; Yan, J.; Wang, L.; Yi, X.; Wang, J.; Zhu, W.; Li, J. Design of AlN ultraviolet metasurface for single-/multi-plane holography. *Appl. Opt.* **2020**, *59* (14), 4398−4403.
(32) Hu, Z.; Long, L.; Wan, R.; Zhang, C.; Zhang, L.; Yan, J.; Duan, H.; Wang, L. Ultrawide bandgap AlN metasurfaces for ultraviolet focusing and routing. *Opt. Lett.* **2020**, *45* (13), 3466−3469.
(33) Miyake, H.; Lin, C.-H.; Tokoro, K.; Hiramatsu, K. Preparation of high-quality AlN on sapphire by high-temperature face-to-face annealing. *J. Cryst. Growth* **2016**, *456* (12), 155−159.
(34) Susilo, N.; Hagedorn, S.; Jaeger, D.; Miyake, H.; Zeimer, U.; Reich, C.; Neuschulz, B.; Sulmoni, L.; Guttmann, M.; Mehnke, F.; Kuhn, C.; Wernicke, T.; Weyers, M.; Kneissl, M. AlGaN-based deep UV LEDs grown on sputtered and high temperature annealed AlN/sapphire. *Appl. Phys. Lett.* **2018**, *112* (4), No. 041110.
(35) Fujikura, H.; Konno, T.; Kimura, T.; Miyake, H. AlN nanostructures and flat, void-less AlN templates formed by hydride vapor phase epitaxy on patterned sapphire substrates. *Appl. Phys. Express* **2020**, *13* (2), No. 025506.
(36) Walde, S.; Huang, C.-Y.; Tsai, C.-L.; Hsieh, W.-H.; Fu, Y.-K.; Hagedorn, S.; Yen, H.-W.; Lu, T.-C.; Weyers, M.; Huang, C.-Y. High-quality AlGaN epitaxy on lattice-engineerable AlN template for high-power UVC light-emitting diodes. *Acta Mater.* **2022**, *226* (3), No. 117625.
(37) Huang, C.-Y.; Walde, S.; Tsai, C.-L.; Netzel, C.; Liu, H.-H.; Hagedorn, S.; Wu, Y.-R.; Fu, Y.-K.; Weyers, M. Overcoming the excessive compressive strain in AlGaN epitaxy by introducing high Si-doping in AlN templates. *Jpn. J. Appl. Phys.* **2020**, *59* (7), No. 070904.
(38) Shojiki, K.; Uesugi, K.; Kuboya, S.; Inamori, T.; Kawabata, S.; Miyake, H. High-quality AlN template prepared by face-to-face annealing of sputtered AlN on sapphire. *Phys. Status Solidi b* **2020**, *258* (2), No. 2000352.
(39) Chen, Z.-Y.; Yan, L.-S.; Pan, Y.; Jiang, L.; Yi, A.-L.; Pan, W.; Luo, B. Use of polarization freedom beyond polarization-division multiplexing to support high-speed and spectral-efficient data transmission. *Light: Sci. Appl.* **2017**, *6* (8), No. e16207.
(40) Xiong, B.; Liu, Y.; Xu, Y.; Deng, L.; Chen, C.-W.; Wang, J.-N.; Peng, R.; Lai, Y.; Liu, Y.; Wang, M. Breaking the limitation of polarization multiplexing in optical metasurfaces with engineered noise. *Science* **2023**, *379* (6629), 294−299.
(41) Arbabi, A.; Horie, Y.; Bagheri, M.; Faraon, A. Dielectric metasurfaces for complete control of phase and polarization with subwavelength spatial resolution and high transmission. *Nat. Nanotechnol.* **2015**, *10* (8), 937−943.
(42) Mueller, J. P. B.; Rubin, N. A.; Devlin, R. C.; Groever, B.; Capasso, F. Metasurface Polarization Optics: Independent Phase

Control of Arbitrary Orthogonal States of Polarization. *Proc. Natl. Acad. Sci. U. S. A.* **2021**, *118* (32), No. 113901.

https://doi.org/10.1021/acsphotonics.4c02575
ACS Photonics 2025, 12, 1235−1242